A Robust Double-Network Polymer Evaporator for Enhanced Solar-Driven Water Purification

Yuan Chen [a,b], Chang Lv [a], Yu-xiang Zhao [b], Wen-kai Zhao [b], Guang-en Fu [b], Jun-yi Han [b], Hao-yong Yang [b], Sheng Wang [a,],and Tao Zhang [b,*]*

Y. Chen, C. Lv, Prof. Dr. S Wang,

[a]School of Materials Science and Engineering, Zhejiang Sci-Tech University, Hangzhou 310018, China

E-mail: wangsheng@zstu.edu.cn; wangsheng571@hotmail.com

Y. Chen, Y. Zhao, W. Zhao, G. Fu, J. Han, H. Yang, Prof. Dr. T. Zhang

[b]State Key Laboratory of Advanced Marine Materials, Ningbo Institute of Materials Technology and Engineering, Chinese Academy of Sciences, Ningbo 315201, China

E-mail: tzhang@nimte.ac.cn

Supplementary Materials

Materials: 2,4,6-Triformylphloroglucinol (TP) (95%), (2,4,6-trioxotriazine-1,3,5(2H,4H,6H)-triyl) tris(hexamethylene) isocyanate (HDI), Polyethylene Glycol 600 (PEG-600) were purchased from Shanghai Bide Pharmatech Co., Ltd. $NiCl_2$ (98%), $ZnCl_2$ (>99%), $Cr(NO_3)_3 \cdot 9H_2O$ (>99%) and $Ga(NO_3)_3$ (>99%) were purchased from Shanghai Macklin Biochemical Co., Ltd.. N,N-Diethylcyclohexanamine, trifluoroacetic acid (99% AR), N-methyl-2-pyrrolidinone (NMP) (>98% AR), 1,4-Dioxane (99% AR), Acetonitrile (＞99% AR), $NaHCO_3$ (99.8% AR), NaCl (99.5% AR), Rhodamine B (RB), Methyl Orange (MO) and $CuCl_2$ (>98%) were purchased from Aladdin Biochemical Technology Co., Ltd. 2,4,6-trimethyl-1,3,5-triazine (TMT) (98%) was purchased from Zesheng Technology Co., Ltd. Mesitylene (97% AR) was purchased from Sahn Chemical Technology (Shanghai) Co., Ltd. Unless otherwise stated, the commercially available reagents and solvents were used without further purification.

Supplementary Methods

Synthesis of sp^2C-CPP (TP-TMT)

To synthesize sp^2C-CPP (TP-TMT), 2,4,6-trimethyl-1,3,5-triazine (TMT, 36.96 mg, 0.3 mmol) and 2,4,6-triformylphloroglucinol (TP, 63.04 mg, 0.3 mmol) were dissolved in a 1:1 (v/v) mixture of mesitylene and 1,4-dioxane (8 mL). Trifluoroacetic acid (2.5 mL) and acetonitrile (0.3 mL) were then added, and the mixture was ultrasonicated to achieve a homogeneous suspension. The resulting suspension was transferred to a Teflon-lined autoclave and subjected to hydrothermal treatment at 150 °C for 72 hours under a nitrogen atmosphere.

After cooling to room temperature, the product was collected by filtration, washed thoroughly with tetrahydrofuran and acetone to remove residual impurities, and air-dried to yield sp²C-CPP (TP-TMT) powder.[1]

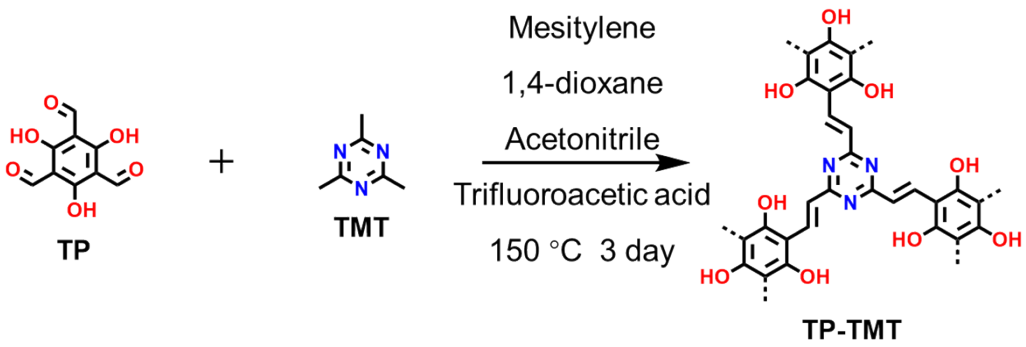

Scheme S1. Schematic representation of the synthesis of TP-TMT sp²C-CPP.

Preparation of NaCl template

NaCl powder was dried in a vacuum oven at 65 °C for 12 hours and then ground into a fine powder. The ground powder was sieved using stainless steel mesh sieves to obtain particles with sizes ranging from 100 to 150 μm.[2]

Preparation of the polymer foam

To prepare the polymer foam, sp²C-CPP (TP-TMT) powder (25 mg) was dispersed in 4 mL of N-methyl-2-pyrrolidone (NMP) by ultrasonication for 40 minutes to form a uniform suspension. Hexamethylene diisocyanate trimer (HDI, 0.5 mL, 3 mmol), polyethylene glycol (PEG-600, 1 g, 1.7 mmol), N,N-diethylcyclohexylamine (3.17 μL, 0.017 mmol), and NaCl template (1 g) were then added to the suspension. The mixture was stirred to ensure complete prepolymerization. The resulting prepolymer solution was carefully poured into a round polytetrafluoroethylene (PTFE) mold (3 cm in diameter) and subjected to a sequential thermal curing process: initially held at 50 °C for 12 hours, then gradually heated to 170 °C over 1 hour, and maintained at 170 °C for an additional 2 hours. The polymer foam was obtained by

removing the NaCl template via ultrasonic washing in deionized water. Finally, the product was dried in a vacuum oven at 70 °C for 24 hours to obtain DN-CPF.[3]

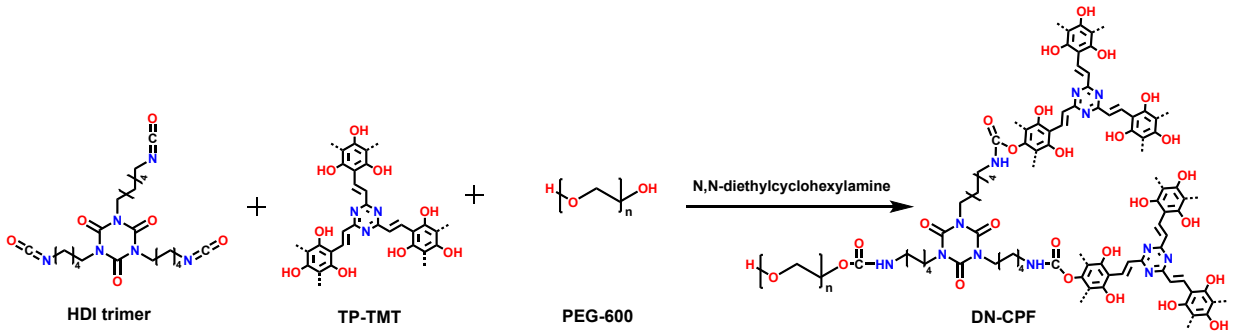

Scheme S2. Schematic representation of DN-CPF synthesis.

Preparation of test solution

Simulated seawater: Simulated seawater was prepared by dissolving NaCl and $NaHCO_3$ in deionized water to achieve a salinity of 3.5 wt%, mimicking natural seawater conditions for solar purification tests.

Heavy metal wastewater: Aqueous solutions containing Cu^{2+}, Cr^{3+}, Zn^{2+}, Ni^{2+}, and Ga^{3+} were prepared by dissolving cupric nitrate, chromic nitrate, zinc chloride, nickel chloride, and gallium nitrate, respectively, in deionized water. The metal ion concentration was set at 500 mg L^{-1} for solar purification experiments.

Organic contaminant solution: Methyl orange (MO) and rhodamine B (RB) solutions were prepared by dissolving the respective dyes in deionized water at a concentration of 20 mg L^{-1} for solar purification tests.

Experimental processes and characterizations

Characterization:

Fourier transform infrared (FT-IR) spectra were recorded using a Thermo NICOLET 6700

spectrometer. Scanning electron microscopy (SEM) images were acquired with a HITACHI S4800 high-resolution cold-field emission SEM. Temperature-time profiles and infrared thermal images of DN-CPF were obtained using an Optris PI400 infrared camera. Hydrophilicity was assessed using a contact angle goniometer (JY-82B Kruss DSA). UV-Vis diffuse reflectance spectra were recorded using a PE Lambda 950 spectrophotometer at room temperature. Mechanical properties were measured using a universal testing machine (UTM 6103, SUNS, China) with a 30 kN load cell, applying a compression rate of 2 mm/min. Thermogravimetric analysis (TGA) was conducted on a Mettler Toledo TGA290 Star System under a nitrogen atmosphere, heating from 25 to 800 °C at 10 °C/min. Differential scanning calorimetry (DSC) measurements were performed on a Netzsch STA 449-F3 Jupiter instrument under a nitrogen flow of 50 mL/min, heating from 25 to 180 °C at 5 °C/min. Inductively coupled plasma mass spectrometry (ICP-MS) analysis was performed using a 715-ES ICP-MS system (Varian).

Photothermal performance evaluation:

The water evaporation rate and solar energy conversion efficiency during the photothermal evaporation process were evaluated using a home-made solar interface photothermal evaporation system. Water evaporation experiments were conducted under controlled conditions at approximately 26 °C and 40% relative humidity using a xenon lamp (PL-X300DF, PLSS) equipped with an AM 1.5G optical filter. The solar intensity was measured using a solar power meter (TES 132-SOLAR). The mass of the evaporated water was determined with an electronic balance (METTLER TOLEDO JJ324BF) with a resolution of 0.1 mg. The final mass change of the water after 1 hour of illumination was recorded to

calculate the evaporation rate (ṁ) using the equation:

$$\dot{m} = \frac{m}{S} \tag{1}$$

Where m is the mass change measured after 1 hour of illumination, and S is the surface area of the DN-CPF. During the solar evaporation process, each sample was submerged in water. The solar photothermal evaporation efficiency (η) was calculated using the following equation:

$$\eta = \frac{\dot{m} h_{LV}}{q C_{opt}} \tag{2}$$

Where ṁ is the water evaporation rate (after subtracting the evaporation rate under dark conditions), h_{LV} is the latent heat of vaporization, q is the nominal solar intensity (1 kW m^{-2}), and C_{opt} is the optical concentration.

Cyclic stability test: After each desalination cycle, the DN-CPF was immersed in deionized water for 12 hours, with the water being refreshed every 2 hours. The system was then reused for the subsequent cycle.

Supplementary Figures

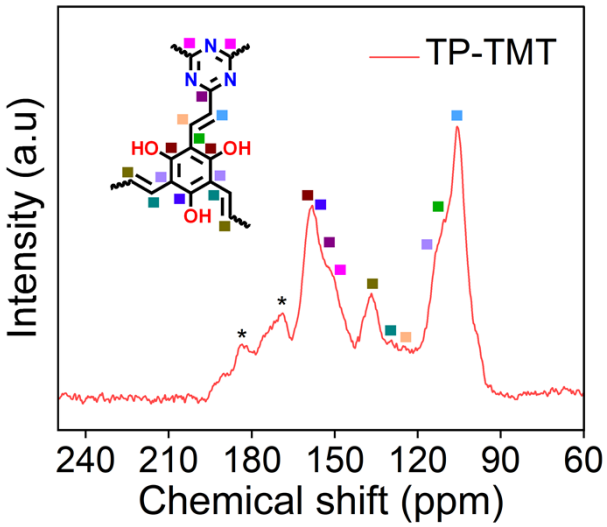

Fig. S1 Solid-state ^{13}C NMR spectrum of TP-TMT. The spectrum confirms the chemical structure of sp^2C-CPP, with characteristic peaks at 124 ppm and 105 ppm corresponding to the newly formed C=C bonds.

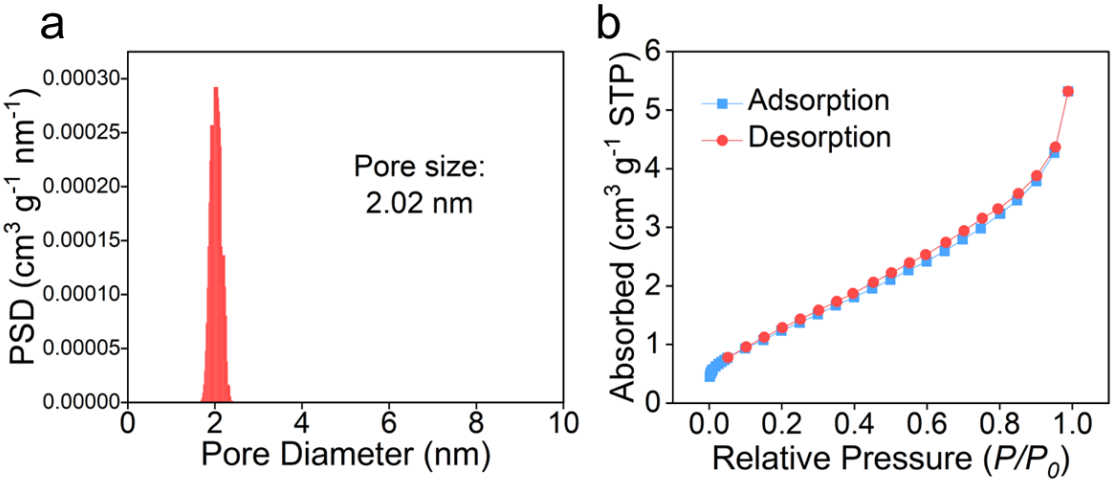

Fig. S2 (a) Pore size distribution of TP-TMT, calculated using quenched solid density functional theory (QSDFT). (b) Nitrogen adsorption and desorption isotherms with pore size distribution of TP-TMT (BET Surface Area: 5.31 m^2 g^{-1}).

N_2 adsorption-desorption measurements at 77 K confirm the presence of mesopores and micropores within the macroporous network. TP-TMT exhibits a pore size of 2.02 nm, as determined by QSDFT. However, in DN-CPF, sp^2C-CPP primarily acts as a crosslinking agent, reacting with the HDI trimer. This reaction results in the filling of the porous network, precluding direct pore size measurement. Nonetheless, the overall porous framework remains rich in hydroxyl and other hydrophilic functional groups, facilitating efficient water transport.

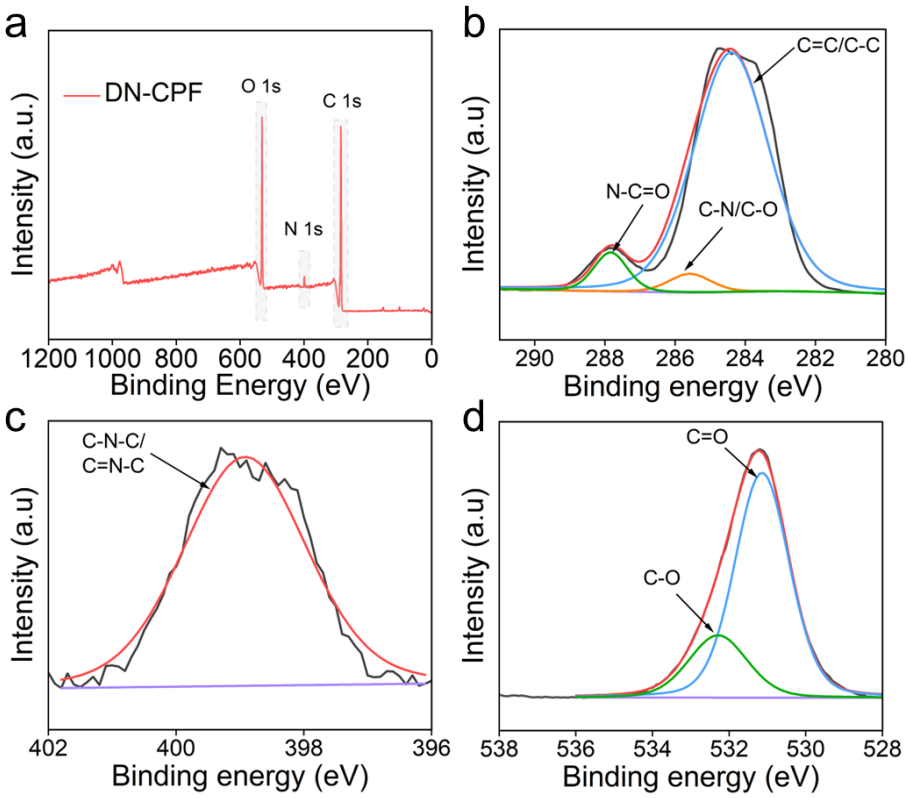

Fig. S3 X-ray photoelectron spectroscopy (XPS) analysis of DN-CPF. (a) XPS survey spectrum of DN-CPF. High-resolution spectra of (b) C 1s, (c) N 1s, and (d) O 1s.

XPS was employed to characterize the chemical composition and bonding states of DN-CPF (Fig. S3a). In the C 1s spectrum (Fig. S3b), the peak at 284.4 eV corresponds to C–C/C=C, while the peaks at 285.6 eV and 287.8 eV are attributed to C–O/C–N and N–C=O, respectively. The N 1s spectrum (Fig. S3c) exhibits a single peak at 398.9 eV, assigned to C–N–C and C=N–C. In the O 1s spectrum (Fig. S3d), the peak at 531.1 eV corresponds to C=O, while the peak at 532.3 eV is attributed to C–O.

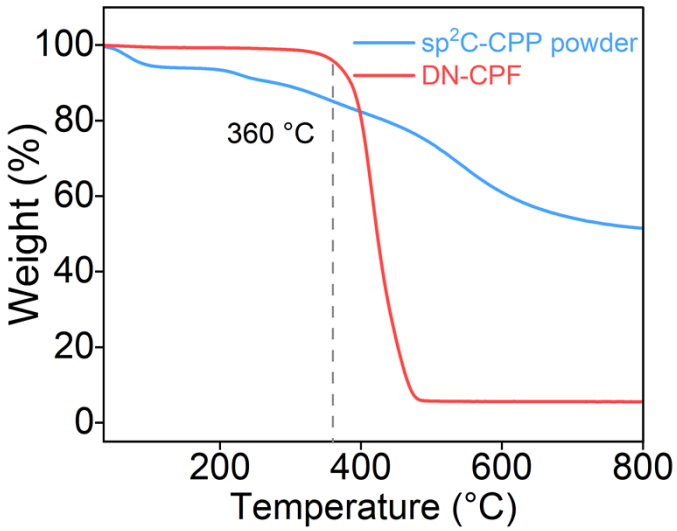

Fig. S4 Thermogravimetric analysis of sp^2C-CPP (blue) and DN-CPF (red). Thermogravimetric analysis (TGA) demonstrated excellent thermal stability of DN-CPF, with less than 5% weight loss at temperatures up to 360 °C.

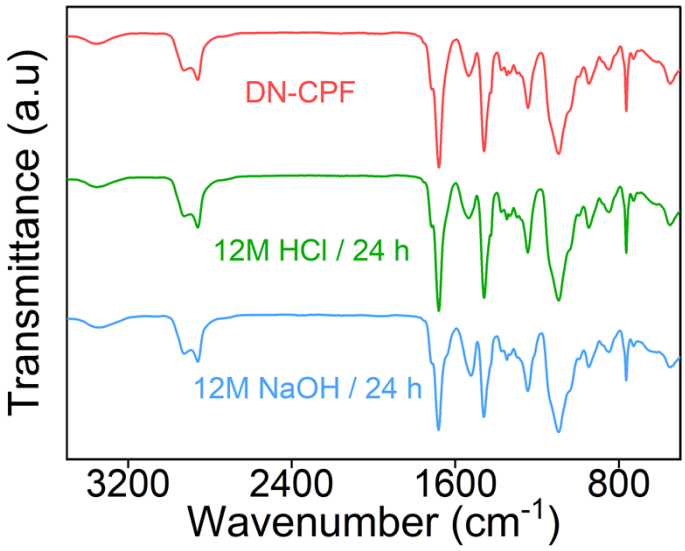

Fig. S5 Comparison of FT-IR spectra of DN-CPF before and after treatment with 12 M HCl and 12 M NaOH for 24 hours.

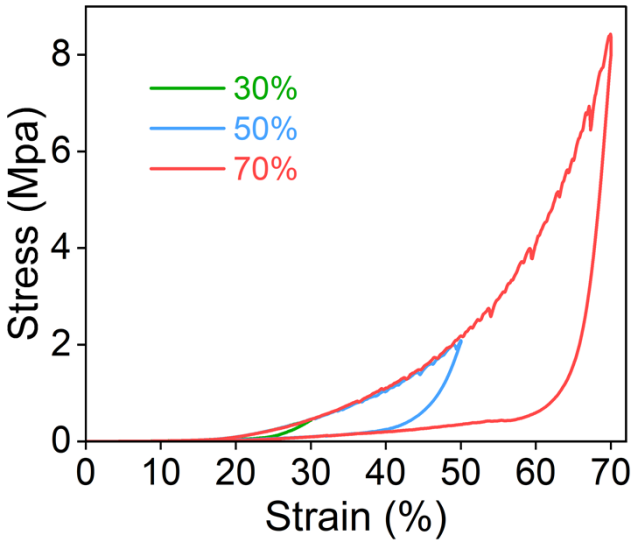

Fig. S6 Compression stress-strain curves of DN-CPF at strains of 30%, 50%, and 70%.

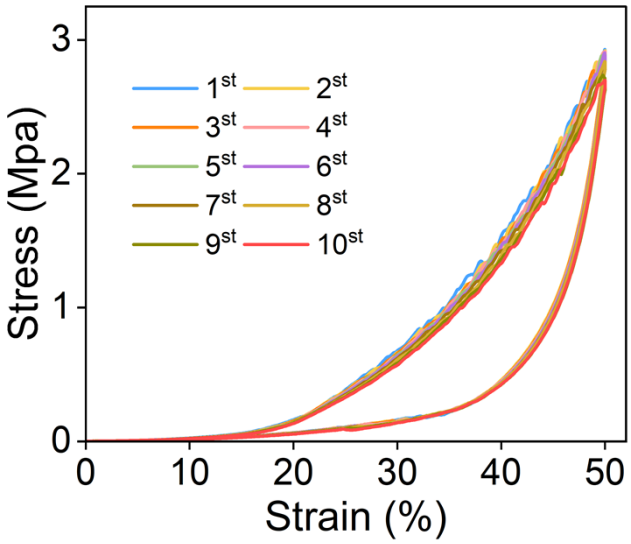

Fig. S7 Cyclic stress-strain curves of DN-CPF at a strain of 50%.

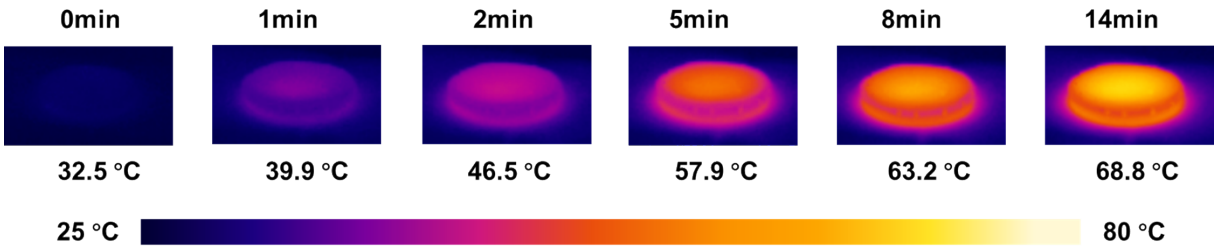

Fig. S8 IR images of DN-CPF under 1 sun irradiation for 14 minutes.

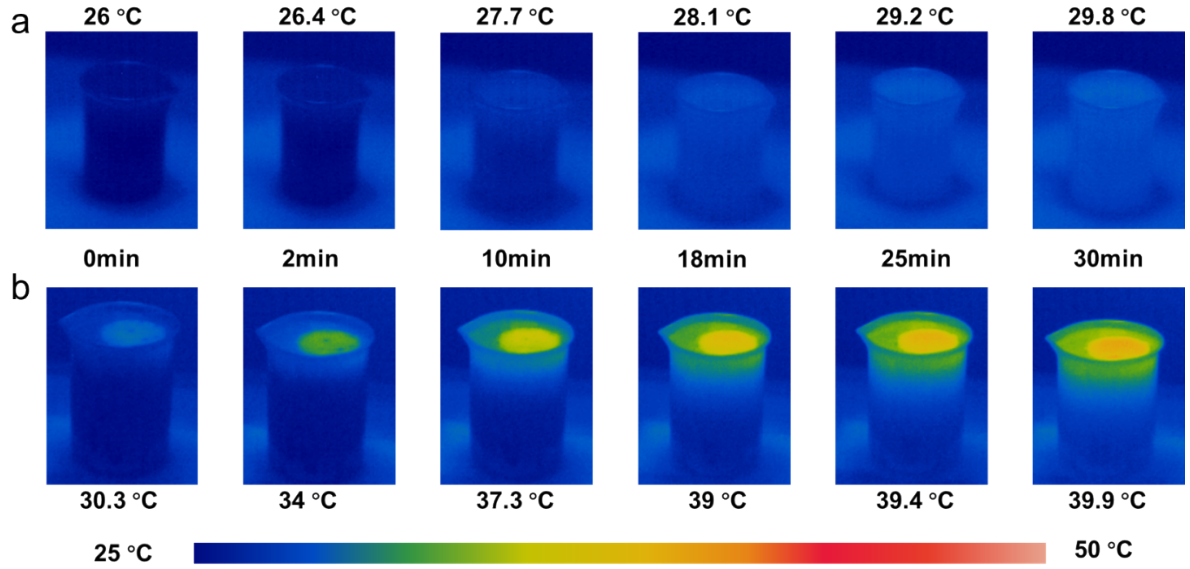

Fig. S9 IR images of (a) bulk water and (b) DN-CPF soaked with water under 1 sun irradiation for 30 minutes.

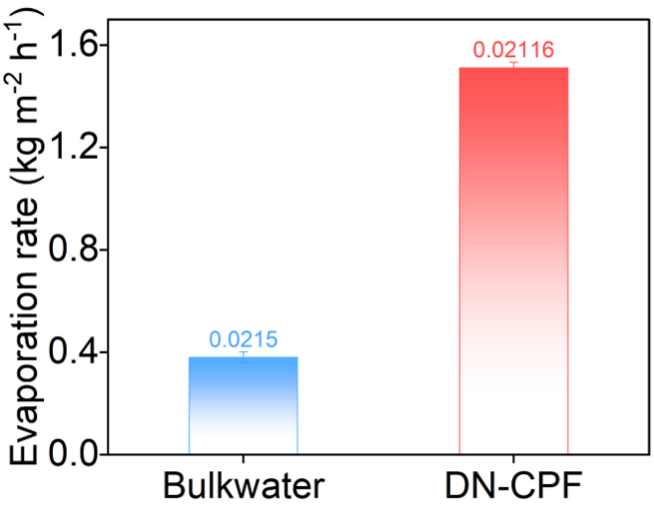

Fig. S10 Comparison of the evaporation rate of bulk water (blue) and DN-CPF (red) under 1 sun irradiation.

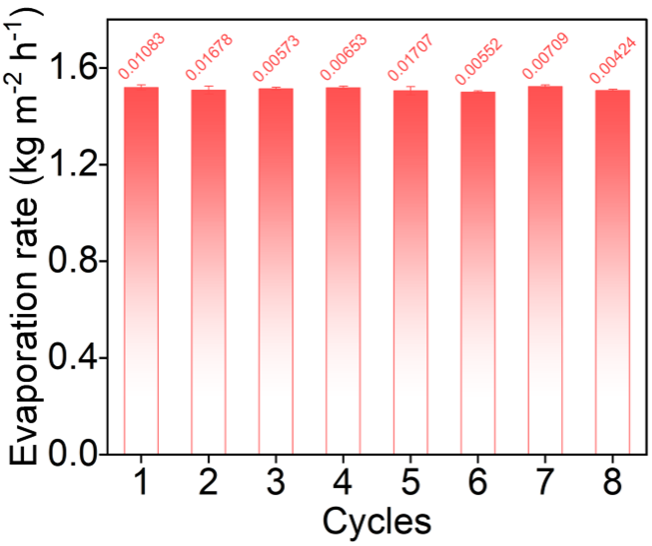

Fig. S11 Stability test of DN-CPF: water evaporation rate over eight consecutive cycles under 1 sun irradiation.

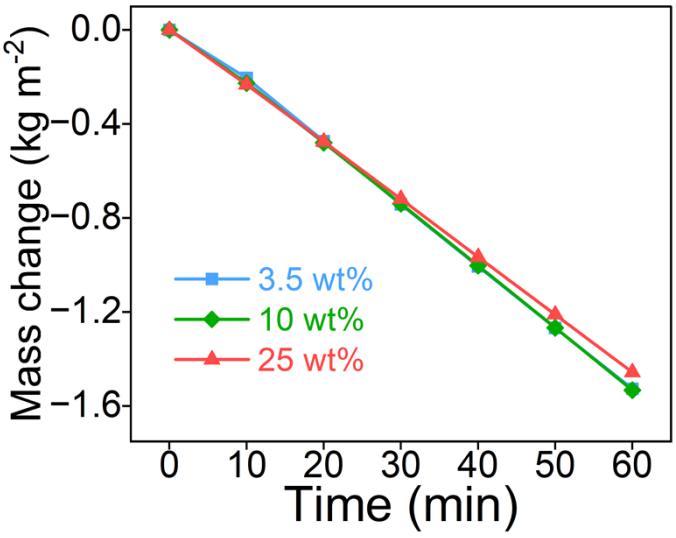

Fig. S12 Mass change curve of DN-CPF in brine with varying concentrations under 1-sun irradiation.

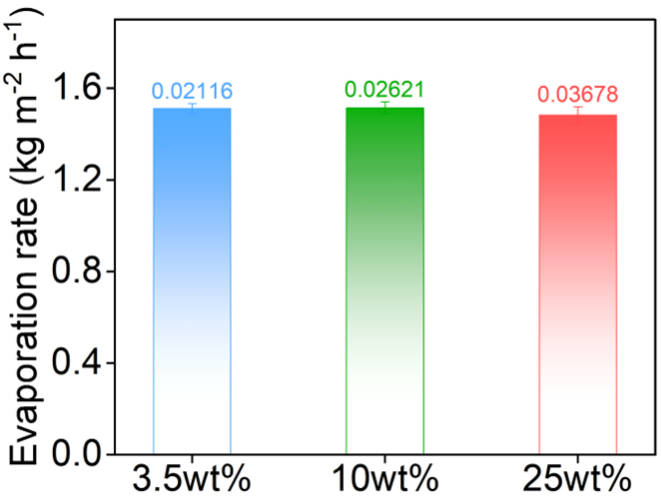

Fig. S13 Water evaporation rate of DN-CPF under varying simulated seawater concentrations.

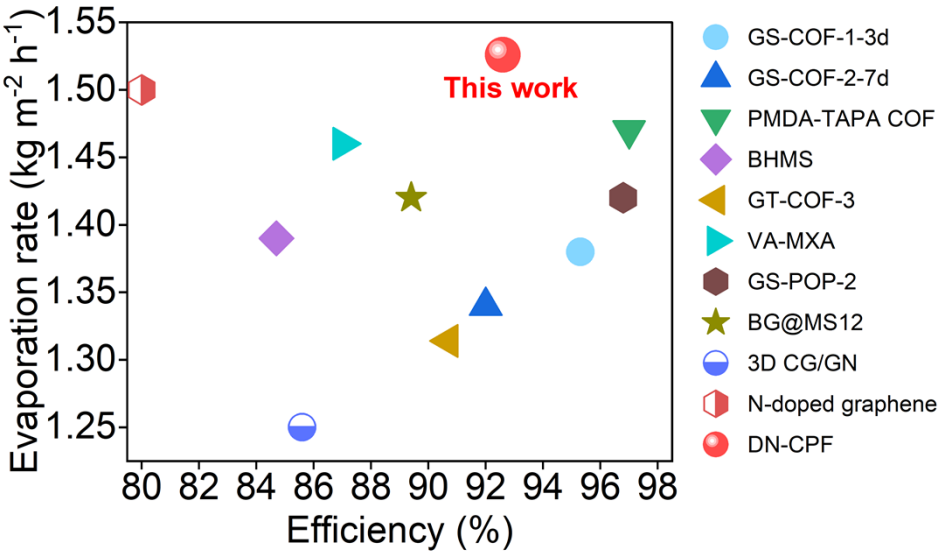

Fig. S14 Comparison of the evaporation performance and photothermal conversion efficiency of DN-CPF with previously reported evaporators.

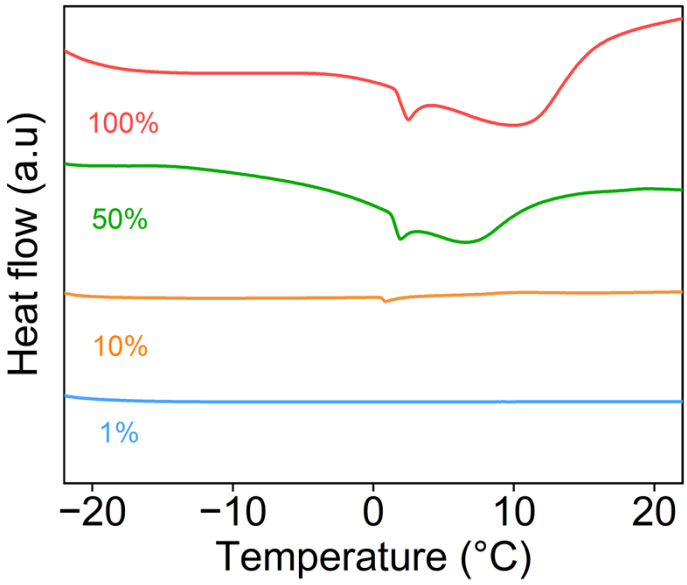

Fig. S15 Differential scanning calorimetry (DSC) curves of the DN-CPF with different water fraction (i.e., swollen level, 100% refers to the fully swollen state).

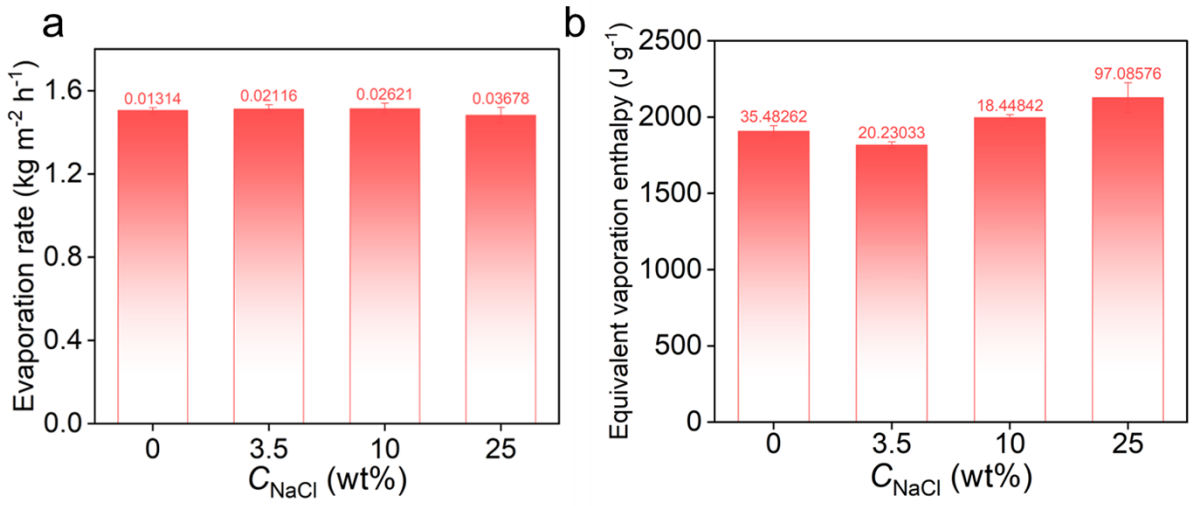

Fig. 16 (a) Evaporation rate at different NaCl concentrations. (b) Calculated equivalent enthalpy of evaporation for different NaCl concentrations.

The enthalpy of evaporation at varying salt concentrations (0 wt%, 3.5 wt%, 10 wt%, and 25 wt%) was measured and analyzed using DSC. The results indicate that as salt concentration increases, both the evaporation rate and enthalpy of evaporation initially decrease and then increase. This trend is attributed to the dual role of salt ions: at lower concentrations, salt ions weaken polymer-water interactions while facilitating water molecule activation, thereby reducing the energy required for evaporation. At higher concentrations, intensified ion-water interactions reduce the proportion of weakly bound water (IW), ultimately affecting the evaporation process.[4,5]

Table S1 Comparison of the evaporation performance and photothermal evaporation efficiency of various evaporator materials reported in previous studies.

Materials	**Evaporation ability ($Kg\ m^{-2}\ h^{-1}$)**	**photothermal evaporation efficiency**	**Reference**
DN-CPF	**~1.526**	**~92.6%**	**This work**
GS-COF-1-3d	~1.38	~95.3%	[6]
GS-COF-2-7d	~1.34	~92%	[6]
PMDA-TAPA COF	~1.47	~97%	[7]
BHMS	~1.39	~84.7%	[8]
GT-COF-3	~1.314	~90.7%	[9]
VA-MXA	~1.46	~87%	[10]
GS-POP-2	~1.42	~96.8%	[11]
BG@MS12	~1.42	~89.4%	[12]
3D CG/GN	~1.25	~85.6%	[13]
N-doped graphene	~1.5	~80%	[14]

Reference

1 R.-H. Xu, W.-R. Cui, C.-R. Zhang, X.-R. Chen, W. Jiang, R.-P. Liang and J.-D. Qiu, *Chem. Eng. J.*, 2021, **419**, 129550.

2 R. Li, M. Wu, H. Ma, Y. Zhu, H. Zhang, Q. Chen, C. Zhang and Y. Wei, *Adv. Mater.*, 2024, **36**, 2402016.

3 M. Wu, Y. Wei, Y. Zhu, Y. Bai, Y. Wang, X. Wang, S.-H. Ho, W. Wang and R. Li, *Adv. Funct. Mater.* 2024, **34**, 2410729.

4 F. Zhu, L. Wang, B. Demir, M. An, Z. L. Wu, J. Yin, R. Xiao, Q. Zheng and J. Qian, *Mater. Horiz.*, 2020, **7**, 3187–3195.

5 C. Lei, W. Guan, Y. Guo, W. Shi, Y. Wang, K. P. Johnston and G. Yu, *Angew. Chem. Int. Ed.*, 2022, **61**, e202208487.

6 Z. Chen, Y. Su, X. Tang, X. Zhang, C. Duan, F. Huang and Y. Li, *Solar RRL*, 2021, **5**, 2100762.

7 X. Li, Y. Pang, Y. Zhang, B. Ge, J. Liu, Y. Zhang, L. Zhao, G. Ren and Z. Zhang, *Sep. Purif. Technol.*, 2023, **326**, 124804.

8 W.-R. Cui, C.-R. Zhang, R.-P. Liang, J. Liu and J.-D. Qiu, *ACS Appl. Mater. Interfaces*, 2021, **13**, 31561–31568.

9 X. Tang, Z. Chen, Q. Xu, Y. Su, H. Xu, S. Horike, H. Zhang, Y. Li and C. Gu, *CCS Chem*, 2022, **4**, 2842–2853.

10 Q. Zhang, G. Yi, Z. Fu, H. Yu, S. Chen and X. Quan, *ACS Nano*, 2019, **13**, 13196–13207.

11 Y. Su, Z. Chen, X. Tang, H. Xu, Y. Zhang and C. Gu, *Angew. Chem., Int. Ed.*, 2021, **60**, 24424–24429.

12 M. Wang, Y. Wei, X. Wang, R. Li, S. Zhang, K. Wang, R. Wang, H. Chang, C. Wang, N. Ren and S.-H. Ho, *Nat. Water*, 2023, **1**, 716–724.

13 Y. Li, T. Gao, Z. Yang, C. Chen, W. Luo, J. Song, E. Hitz, C. Jia, Y. Zhou, B. Liu, B. Yang and L. Hu, *Adv. Mater.*, 2017, **29**, 1700981.

14 Y. Ito, Y. Tanabe, J. Han, T. Fujita, K. Tanigaki and M. Chen, *Adv. Mater.*, 2015, **27**, 4302–4307.